catalysts

MDPI

Article

Electrocatalytic Pathways and Efficiency of Cuprous Oxide (Cu_2O) Surfaces in CO_2 Electrochemical Reduction (CO_2ER) to Methanol: A Computational Approach

Zubair Ahmed Laghari [1], Wan Zaireen Nisa Yahya [1,*], Sulafa Abdalmageed Saadaldeen Mohammed [2] and Mohamad Azmi Bustam [1]

[1] Department of Chemical Engineering, Centre of Research in Ionic Liquids, Universiti Teknologi PETRONAS, Seri Iskandar 32610, Perak, Malaysia; zubair_22008648@utp.edu.my (Z.A.L.); azmibustam@utp.edu.my (M.A.B.)
[2] Department of Energy Technology, Aalborg University, 9220 Aalborg, Denmark; sasm@energy.aau.dk
* Correspondence: zaireen.yahya@utp.edu.my

Abstract: Carbon dioxide (CO_2) can be electrochemically, thermally, and photochemically reduced into valuable products such as carbon monoxide (CO), formic acid (HCOOH), methane (CH_4), and methanol (CH_3OH), contributing to carbon footprint mitigation. Extensive research has focused on catalysts, combining experimental approaches with computational quantum mechanics to elucidate reaction mechanisms. Although computational studies face challenges due to a lack of accurate approximations, they offer valuable insights and assist in selecting suitable catalysts for specific applications. This study investigates the electrocatalytic pathways of CO_2 reduction on cuprous oxide (Cu_2O) catalysts, utilizing the computational hydrogen electrode (CHE) model based on density functional theory (DFT). The electrocatalytic performance of flat Cu_2O (100) and hexagonal Cu_2O (111) surfaces was systematically analysed, using the standard hydrogen electrode (SHE) as a reference. Key parameters, including free energy changes (ΔG), adsorption energies (E_{ads}), reaction mechanisms, and pathways for various intermediates were estimated. The results showed that CO_2 was reduced to $CO_{(g)}$ on both Cu_2O surfaces at low energies. However, methanol (CH_3OH) production was observed preferentially on Cu_2O (111) at $\Delta G = -1.61$ eV, whereas formic acid (HCOOH) and formaldehyde (HCOH) formation were thermodynamically unfavourable at interfacial sites. The CO_2-to-methanol conversion on Cu_2O (100) exhibited a total ΔG of -3.38 eV, indicating lower feasibility compared to Cu_2O (111) with $\Delta G = -5.51$ eV. These findings, which are entirely based on a computational approach, highlight the superior catalytic efficiency of Cu_2O (111) for methanol synthesis. This approach also holds the potential for assessing the catalytic performance of other transition metal oxides (e.g., nickel oxide, cobalt oxide, zinc oxide, and molybdenum oxide) and their modified forms through doping or alloying with various elements.

Keywords: CO_2 electrochemical reduction; copper oxide electrocatalyst; methanol production; DFT studies

check for updates

Academic Editor: Zhixin Yu

Received: 20 December 2024
Revised: 23 January 2025
Accepted: 24 January 2025
Published: 29 January 2025

Citation: Laghari, Z.A.; Yahya, W.Z.N.; Mohammed, S.A.S.; Bustam, M.A. Electrocatalytic Pathways and Efficiency of Cuprous Oxide (Cu_2O) Surfaces in CO_2 Electrochemical Reduction (CO_2ER) to Methanol: A Computational Approach. *Catalysts* **2025**, *15*, 130. https://doi.org/10.3390/catal15020130

Copyright: © 2025 by the authors. Licensee MDPI, Basel, Switzerland. This article is an open access article distributed under the terms and conditions of the Creative Commons Attribution (CC BY) license (https://creativecommons.org/licenses/by/4.0/).

1. Introduction

Carbon dioxide (CO_2) emission is a significant issue contributing to climate change and environmental pollution [1,2]. Consequently, carbon capture, utilization, and storage (CCUS) technologies have been widely developed and employed to reduce CO_2 emissions [3,4]. Among CO_2 utilization technologies, thermal, photochemical, and electrochemical CO_2 reductions are extensively explored for converting CO_2 into fuels and value-added

chemicals. CO_2 electrochemical reduction (CO_2ER) presents a potentially sustainable and stable technique. Nonetheless, these approaches are yet to be implemented industrially due to their considerable energy consumption and low product yield.

Turning CO_2 via CO_2ER into fuels and chemicals highly depends upon the electrolytes and catalysts used [5]. Multiple products can be formed in CO_2ER, such as formic acid (HCOOH), carbon monoxide (CO), methane (CH_4), ethylene (C_2H_4), and methanol (CH_3OH) [6]. CH_3OH conversion on one side is significantly advantageous among these products due to its high market value. However, it also entails a complex reaction pathway in CO_2ER requiring six electron–proton transfers, contrary to the formation of other products, that involve only one or two electron transfers, such as HCOOH or CO [7].

CH_3OH, which is employed industrially as a solvent, pesticide, and alternative fuel source [8], can also be stored in fuel cells, offering direct and convenient internal combustion systems [9]. The demand for CH_3OH has been increasing for various hydrocarbon applications. The total output capacity of CH_3OH was recorded at over 138 billion litres from 2015 to 2020 while CH_3OH utilization increased from 40% to 60% in emerging energy applications [10]. Approximately 250,000 tons of CH_3OH are employed daily as a chemical feedstock or transportation fuel. Producing CH_3OH through CO_2ER can be cost-effective by improving the current density, reducing the system's energy consumption using more active catalysts, and increasing the ionic conductivity of the electrolytes. Consequently, enhancing CH_3OH production via CO_2ER can have multidimensional benefits [11].

In CO_2ER, CO_2 is reduced through a redox reaction in an electrochemical cell, which yields different products at various potentials, some of the examples are provided in Equations (1)–(5), with their respective standard potentials relative to a standard hydrogen electrode (SHE) [12–15]. CH_3OH has less negative potential as compared to formic acid and carbon monoxide but requires higher electron–proton transfer, making it more challenging to achieve higher efficiency and selectivity.

$$CO_2 + 2H^+ + 2e^- \rightarrow HCOOH \quad (-0.61\ V) \tag{1}$$

$$CO_2 + 2H^+ + 2e^- \rightarrow CO + H_2O \quad (-0.53\ V) \tag{2}$$

$$CO_2 + 6H^+ + 6e^- \rightarrow CH_3OH + H_2O \quad (-0.38\ V) \tag{3}$$

$$CO_2 + 12H^+ + 12e^- \rightarrow C_2H_4 + 4H_2O \quad (-0.34\ V) \tag{4}$$

$$CO_2 + 8H^+ + 8e^- \rightarrow CH_4 + 2H_2O \quad (-0.24\ V) \tag{5}$$

CO_2 absorption in the electrolyte and adsorption/desorption at the electrode interface also involve complex reactions, thus developing an efficient system for reducing overpotential with a high methanol production rate is challenging [16,17]. Active electrocatalysts and electrolytes are necessary to improve product yield and decrease energy consumption during CO_2ER [18–20]. Accordingly, miscellaneous catalysts have been assessed for CO_2 conversion into different products [21,22]. Studies have found that metal oxides [23], bimetals [24], and alloys [25] are more feasible electrocatalysts than pure metals to produce fuels, hydrocarbons, and alcohol-based products through CO_2ER [26].

A multicomponent electrocatalyst consisting of silver/sulphur-cuprous oxide/copper (Ag/S-Cu_2O/Cu) demonstrated a CH_3OH production at a 67.4% faradic efficiency (FE) with the presence of ionic liquid in the electrolyte [27,28]. In another report, ethanol was successfully produced with a 40.8% FE employing Ag/Cu_2O electrocatalyst [29]. On the other hand, gold (Au) nanowires were reported to produce CO at 94% FE [30]. Following CO_2 saturation, potassium bicarbonate ($KHCO_3$) recorded excellent FE for alcohol-based products when the Ag/Cu electrodes were prepared through sputtering deposition [31].

Oxides composed of cations and anions have more diverse surface morphologies, compositions, and structures than metals [32]. The atomic arrangement and composition of oxides result in varying activities for different reaction coordinates. Consequently, product desorption primarily depends on the nature of the catalyst surface and its interaction with the electrolytes.

Several computational techniques have been applied to correlate the performance of the electrodes and electrolytes [33,34], effective sorption energies, and the effects of variables on the reaction pathways to understand the CO_2ER mechanism on the atomic scale [35–38]. Producing HCOOH directly from *OCHO hydrogenation on Cu_2O (100) surfaces has been documented with excellent accuracy [39]. Furthermore, the ideal $CO_2 \rightarrow$ *COOH $\rightarrow$ *CO $\rightarrow$ CO pathway was obtained with Cu (111) and CuO (111), where * represents the adsorption site of the catalyst [40,41].

Chu et al. demonstrated through experimental and density functional theory (DFT) calculations that ethylene (C_2H_4) was the principal product when antimony (Sb)-modified CuO catalysts were employed [42]. The hydrogenation sequence on copper single-atom alloy for carbon monoxide (CO) production follows CO_2 + * $\rightarrow$ *CO_2 $\rightarrow$ *COOH $\rightarrow$ *CO + H_2O $\rightarrow$ CO pathway [43]. Meanwhile, CH_4 follows the longer pathway CO_2 + * $\rightarrow$ *CO_2 $\rightarrow$ *COOH $\rightarrow$ *CO + H_2O $\rightarrow$ *HCO $\rightarrow$ *H_2CO $\rightarrow$ *H_3CO $\rightarrow$ CH_4 + *O, where H_3CO* can be hydrogenated into CH_3OH with additional potential [44].

Electrocatalyst facets possess a considerable influence on electrochemical reduction catalytical activities and stability [45,46]. Consequently, establishing the role of crystal facets is critical during CH_3OH activity and selectivity on catalyst surface determinations. Hence, various computational models are used to estimate the effective potentials in the gas–liquid–solid interface. The effective DFT energies, charge densities, and thermal properties, relevant to catalysts are usually determined using constant electrode potential (CEP), Grand Canonical DFT (GC-DFT), and computational hydrogen electrode (CHE) [47]. CEP normally works on the C–C coupling stage consisting of non-redox processes influenced by the applied voltage [48]. A report estimates that the predictions of the CHE model are adequate for studies involving redox reactions, HER, or OER under DFT energies. The CEP model is suitable for studying complex structures that demand the use of external potential, and it focuses on proton-coupled electron transfer (PCET) steps [49]. The CEP model considers the change in the number of electrons in the unit cell and allows fractional value as constant potential. This increases the computational cost and effort because of the need for iterative DFT calculations at each value of the applied bias. To our knowledge, the CEP has not been extensively utilized to model the CO_2ER, in contrast to the commonly employed CHE [50]. Additionally, the GC-DFT method is computationally intensive, as it accounts for the potential and surface charges of the entire system, recalculating each potential during simulations with reduced precision for free energy values.

In this study, a computational hydrogen electrode (CHE) model with a semi-hydrogen $H_{2(g)}$ reference electrode and a copper-oxide catalyst (Cu_2O) with different facets are employed during the assessments. Several types of energies have been derived through density functional theory (DFT) by solving the gas–liquid–solid interface system according to the electrochemical cell standards. Primarily, product desorption depends upon the nature of the catalyst surface and electrolyte in the system. Nevertheless, other electrolytes can also be introduced with the reference $H_{2(g)}$ molecule layer [51,52].

Catalyst active site selectivity can be significantly improved with computational calculations [53]. This study employed DFT, combining quantum mechanical insights with dynamic molecular simulations to provide a more comprehensive analysis to assess transition states and potential variations during CO_2ER in different coordinates. During the reactions, CO_2 as the reactant undergoes transition states yielding various products. DFT

calculations utilizing the CHE model also enabled evaluations of reaction types, energy states, and density of states in the system [45,54,55].

The direct correlation of DFT energies to the actual potential (voltage) of a system using Cu_2O (111) and (100) surfaces is still unknown. These two facets of Cu_2O vary in atomic densities and atomic arrangements, which alternatively made a significant impact on selectivity and catalytic activity. Simplifying the engineering of these surfaces, understanding binding energies (how strongly intermediates attach to the surface), and the transition from non-spontaneous to spontaneous reactions for each intermediate is crucial for understanding the stability and selectivity of Cu_2O. However, these aspects have not been thoroughly reported in the literature. Additionally, the CO_2 adsorption and activation between these two surfaces are different and are not well characterized. To the best of our knowledge, this is the first instance of a detailed discussion employing DFT to examine the influence of geometrical variations on binding and adsorption-desorption phenomena from angles to length variation for each intermediate. Furthermore, understanding the mechanisms at the interface between a solid catalyst and a liquid electrolyte, where the electrolyte helps transport gas molecules to the catalyst, is challenging.

This study aims to predict and understand the electrocatalytic properties of CO_2ER to C_1 products (notably CH_3OH) over Cu_2O (100) and Cu_2O (111) catalysts using the CHE model by assessing the sequential hydrogenation pathways. The present study determined the changes in the reaction-free energies, adsorption energies, reaction pathways, and shortest sites for CH_3OH formation including adsorbate behaviour on these facets in detail. The hydrogen molecule was employed as the reference electrode, which maintained the proton and electron transfer values in the elementary steps and helped standardize the measurements and comparisons. The findings demonstrate that the selectivity and product yield depend on the crystallographic planes and the active sites of the catalyst.

2. Results and Discussion

2.1. Models and Molecular Activation on Cu_2O (100) and Cu_2O (111) Sites

The varying behaviours of the adsorbates following DFT calculations on cuprous oxide facets Cu_2O (100) and Cu_2O (111) are illustrated in Figures 1 and 2, respectively. The change in adsorbates' geometries before and after interaction with the catalyst are given in Table 1. The colours white, red, black, and orange-red were assigned to hydrogen, oxygen, carbon, and copper atoms, respectively, while the dimensions are reported in Angstrom (Å) for length, and degree for angle. The structural diversions of different adsorbates and CO_2 on the flat Cu_2O (100) and hexagonal Cu_2O (111) surfaces were determined, and the change on (100) and (111) surfaces was also discussed.

The standard molecular dimensions were confirmed through different databases, including Materials Project, PubChem, and the Crystallography Open Database (COD) [56–58]. Structural deviations indicate the catalytic activities of the catalyst interacting with different absorbates. The Cu-O-Cu in both Cu_2O (100) and Cu_2O (111) shows a constant angle of 109.5° after geometry optimization; however, Cu_2O (100) exhibits higher angle changes as compared to Cu_2O (111). Details in dimension changes for facets are given in Table S1 [59,60].

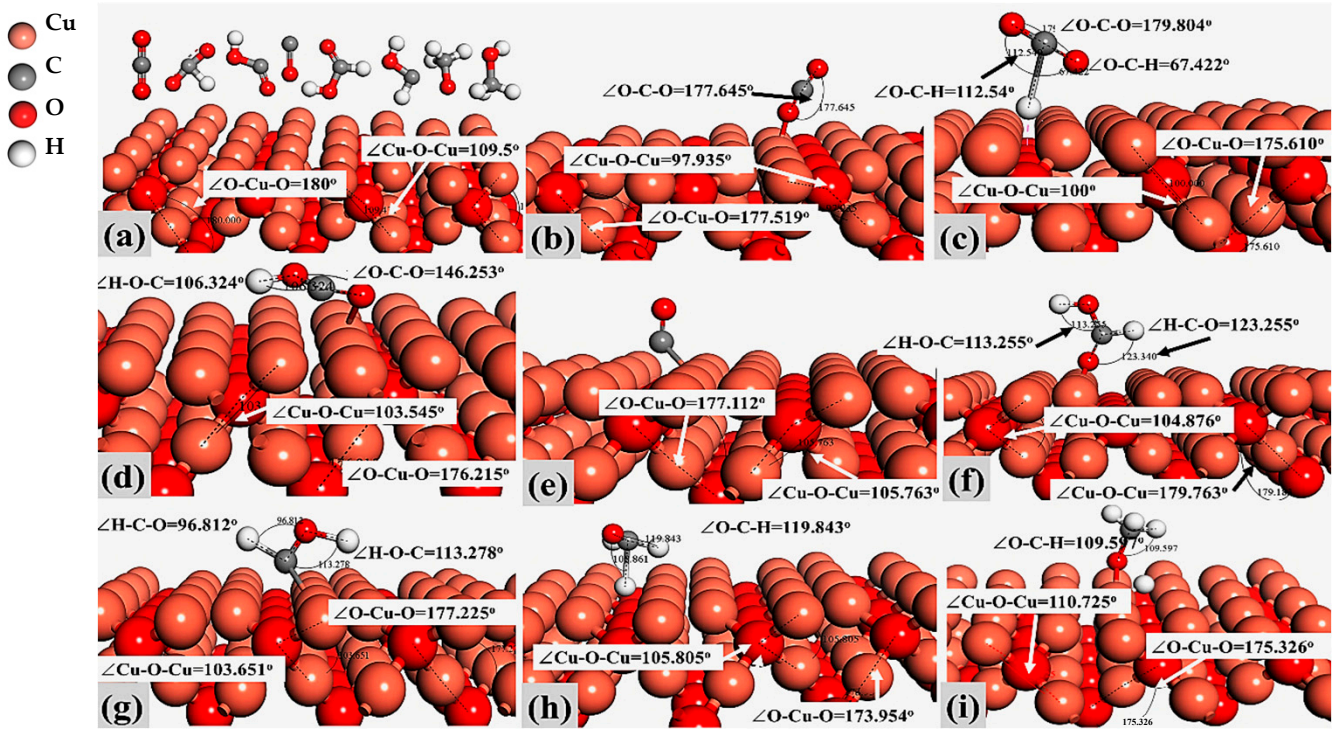


Figure 1. The representations following activation and interaction of the Cu_2O (100) site with different adsorbates after geometry optimization; (**a**) original dimension of Cu_2O (100) and structures of adsorbates, (**b**) *CO_2, (**c**) *HCOO, (**d**) *COOH, (**e**) *CO, (**f**) *HCOOH, (**g**) *HCOH, (**h**) *H_3CO, and (**i**) *CH_3OH.

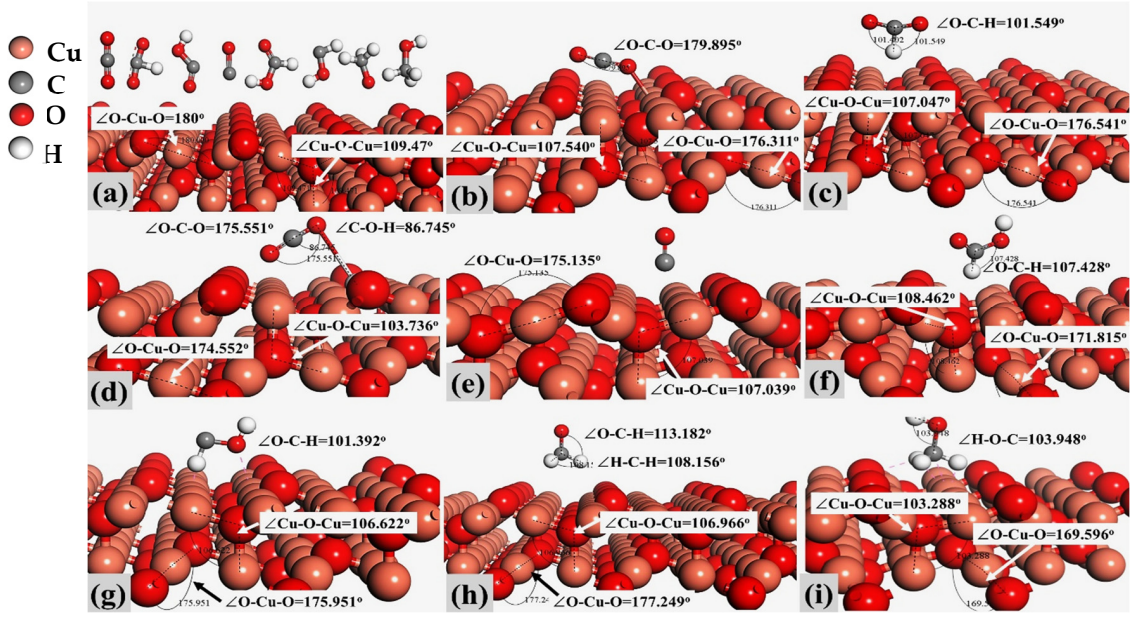
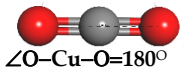
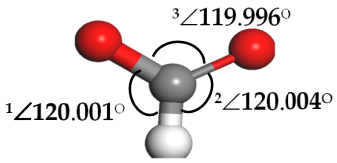
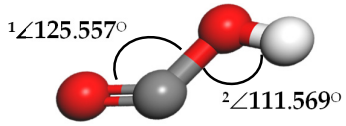
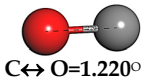
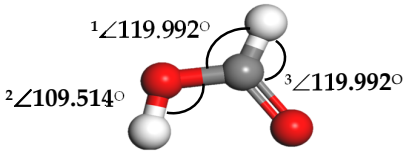
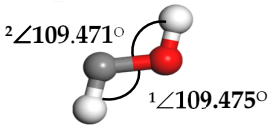
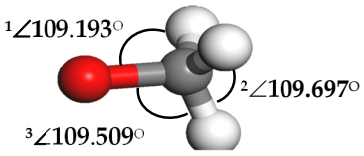
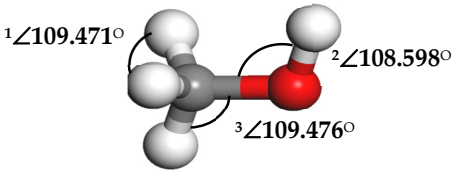


Figure 2. The representations following activation and interaction of the Cu_2O (111) site with different adsorbates after geometry optimization; (**a**) Original dimension of Cu_2O (111) and structures of adsorbates, (**b**) *CO_2, (**c**) *HCOO, (**d**) *COOH, (**e**) *CO, (**f**) *HCOOH, (**g**) *HCOH, (**h**) *H_3CO, and (**i**) *CH_3OH.

Table 1. Details of CO_2 and other adsorbates geometrical variations after interaction on Cu_2O (100) and Cu_2O (111) surfaces.

Compound Name	Compound Structure	After Activation on Cu_2O (100)	After Activation on Cu_2O (111)
Carbon dioxide (CO_2)		∠O–Cu–O = 177.645°	∠O–Cu–O = 179.895°
Formate (HCOO)		^{1}∠H–C–O = 112.549° ^{2}∠H–C–O = 67.422° ^{3}∠O–C–O = 179.807°	^{1}∠H–C–O = 101.402° ^{2}∠H–C–O = 101.549° ^{3}∠O–C–O = 157.048°
Carboxyl (COOH)		^{1}∠O–C–O = 146.253° ^{2}∠C–O-H = 106.324°	^{1}∠O–C–O = 175.551° ^{2}∠C–O–H = 86.745°
Carbon Monoxide (CO)		C↔ O = 1.140°	C↔ O = 1.153°
Formic Acid (HCOOH)		^{1}∠H–O–C = 113.255° ^{2}∠O–C–H = 104.742° ^{3}∠H–C–O = 123.340°	^{1}∠H–O–C = 106.827° ^{2}∠O–C–H = 107.428° ^{3}∠H–C–O = 125.390°
Hydroxymethylene (HCOH)		^{1}∠H–O–C = 113.278° ^{2}∠H–C–O = 96.812°	^{1}∠H–O–C = 107.966° ^{2}∠H–C–O = 101.392°
Methoxy (H_3CO)		^{1}∠H–C–O = 108.861° ^{2}∠H–C–O = 119.843° ^{3}∠H–C–O = 123.132°	^{1}∠H–O–C = 108.156° ^{2}∠H–C–O = 110.627° ^{3}∠H–C–O = 113.182°
Methanol (CH_3OH)		^{1}∠H–C–H = 107.87° ^{2}∠H–O–C = 108.644° ^{3}∠O–C–H = 142.048°	^{1}∠H–C–H = 106.152° ^{2}∠H–O–C = 103.948° ^{3}∠O–C–H = 106.581°

In the case of CO_2ER, the higher adsorption of reaction coordinates negatively impacts selectivity and efficiency towards higher electron–proton transfer for selective products, like in the case of CH_3OH production [61,62]. The higher adsorption in most of the adsorbates for Cu_2O (100) with $*CO_2$, $*H_3CO$, and $*CH_3OH$ recorded the highest O-Cu-O angle differences with 177.519°, 173.954°, and 175.326 as shown in Figure 1. This entity possesses the capability to facilitate one or two electron–proton transfers, ultimately resulting in the formation of the carboxyl functional group (COOH) or $CO_{(g)}$ through $CO_2 + * \rightarrow *CO_2 \rightarrow *COOH \rightarrow *CO + H_2O \rightarrow CO_{(g)}$ with extra energy to proceed for the reaction. The (100) surface has also less non-stoichiometric O termination, making this surface unstable during CO_2ER. The (100) surface, in this case, is reactive and prone to noticeable changes in atomic locations, bond angles, and surface shape, and can be degraded rather than proceeding with an electrochemical reduction reaction. Moreover, minimal changes on the same surface were recorded for *CO, *HCOOH, and *HCOH. The major reason for the unstable (100)

surface is its low oxygen coverage with less than 0.5 monolayer (ML), with the top layer being occupied with Cu, which can move down during the reaction, and the O atomic layer taking part to activate the adsorbates for the reaction. As a result of the electronegativity difference, the O attracts the shared electrons more strongly towards H to form a polar covalent bond, compared to the Cu, which has delocalized electrons and needs additional forces to bind with H, namely temperature, pressure, and pH.

However, the Cu_2O (111) top surface has an O layer available for H exposure, making Cu atoms more stable on this surface for catalytical activity [61–63]. This is also validated by the positive free energy (ΔG) values and non-spontaneous reactions for *CO and *HCOH on Cu_2O (111). The higher tendency of O bonding towards Cu from various adsorbates in Cu_2O (100) can oxidize the Cu surface, leading to copper hydroxide ($Cu(OH)_2$) and copper carbonate ($CuCO_3$) formation that reduces the lifespan of the catalyst rather than alleviating the CO_2ER, which has also been witnessed in multiple research works [64]. Furthermore, the considerable CO-CO interactions induced rearrangements in the Cu_2O structure, requiring more energy to further CO conversions into HCOOH and HCOH [65,66].

The pristine, (defect-free) Cu_2O (111) surfaces employed in this study showed varying catalytic activities due to the dangling coordinatively unsaturated copper (CuU) atom bonds on the Cu_2O (111) surfaces, making them more catalytically active [67]. The non-polar stoichiometric oxygen-terminated surface of Cu_2O (111) exhibited more stability as shown in Figure 2a [67–69]. The highest structure change in O-Cu-O for Cu_2O (111) was seen for *COOH, *HCOOH, and *CH_3OH, while the least changes were recorded for *CO_2, *HCOO, and *H_3CO. The ∠O-Cu-O angle for *CH_3OH on Cu_2O (100) was recorded at 175.326° and Cu_2O (111) exhibited an angle of 169.569°. On the other hand, the Cu-O-Cu change in angle for *CH_3OH was 110.725° for Cu_2O (100) and 103.228° for Cu_2O (111). These variations in Cu_2O (111) for CH_3OH are due to flexible Cu in the catalyst and strong hydroxyl (-OH) bonding towards Cu atoms from methanol. This change is based on the structure relaxation and rearrangement of Cu and O to minimize overall energy in the final product.

The *CH_3OH shows higher adsorption in Cu_2O (100) as illustrated in Figure 1i, which entirely changes the structure of CH_3OH and makes it difficult to stabilize and detach from the surface. The change in the angle of O-C-H in CH_3OH after optimization was measured at 142.048° on Cu_2O (100), which is much higher than the (111) surface. Due to the larger angle and structural changes, CH_3OH becomes unstable on the Cu_2O (100) surface. This instability increases the likelihood that *CH_3OH will dissociate into carbon monoxide (CO) gas or methoxy (H_3CO) rather than forming $CH_3OH_{(l)}$.

The standard angle of O=C=O for CO_2 is found to change from 180° to 177.645° at the Cu_2O (100) surface and to 179.895° on the Cu_2O (111) surface. The Cu_2O (100) is more reactive with less coordinated atoms, and additional unsaturated bonds interact with adsorbed CO_2 molecules leading to greater distortion in CO_2 molecules. It enhances the weakening of the C-O bond and can be slightly better for CO_2 activation than the (111) surface, with the latter consuming more energy during initial reduction. Therefore, the reaction from *CO_2 to *COOH was also determined to be more promising on the (100) surface following the free energy profile. The H stretching in *HCOO and *COOH towards Cu atoms were noted on (100) and (111) surfaces, respectively, which helps to catalytically decompose *HCOO and *COOH towards CO with the highest angle variation in H-C-O of 67.422° in *HCOO on (100) surface, and C-O-H of 86.745° in *COOH for (111) surface (see Table 1).

The $CO_{(g)}$ was found to be stable on both surfaces with minor changes in length. In the case of *HCOOH, the O forming the bond with the Cu atom was found with the highest change on the (100) surface, increasing the angle from 109.514° to 104.742° for

∠O–C–H. Meanwhile, for the (111) surface, the change was observed from 109.514° to 107.428°. Therefore, the desorption of $HCOOH_{(l)}$ from adsorbed *HCOOH on the (111) surface must be higher. Similarly, the variation in angle for H–C–O for *HCOH and $*H_3CO$ computed after adsorption was 96.812° and 123.132° on the Cu_2O (100) and (111) surfaces, respectively. This phenomenon involved carbon (C) bonding from *HCOH towards Cu. In bulk, this can lead to the formation of $CuCO_3$ on the surface, producing H_2O molecules in the electrolyte as a by-product (see Figure 1).

Similar but less pronounced changes were observed on the Cu_2O (111) surface. This suggests that the catalytic conversion of adsorbed molecules occurs more stably without distorting the surface. Therefore, the catalytic activity for converting CO_2 to CH_3OH is more promising on Cu_2O (111) compared to Cu_2O (100).

2.2. Adsorption Energies (E_{ads})

The adsorption energies (E_{ads}) and thermodynamic properties of the different species and catalysts evaluated in the present study were calculated at standard temperature and pressure (298 K and 1 atm) (see Tables S2–S4 in the Supplementary Materials). After geometry optimization, hydrogen gas (H_2) exhibited the lowest heat capacity of 6.99 J/K and an enthalpy of 4.57 kcal/mol, indicating that it has the lowest formation enthalpy among the substances studied [70]. On Cu_2O (100) and (111), the thermodynamic characteristics of various adsorbates revealed a precisely proportional relationship between molar masses and free energies. The E_{ads} obtained in this study were determined following the equations given in Supporting Information Equations (S1)–(S8). According to the results given in Figure 3, the more negative adsorption energies (E_{ads}) lead to higher exergonic rates (more spontaneous) and require more potential than their positive counterparts, requiring more potential to drive CO_2 reduction. Consequently, the adsorption energy is inversely related to the free energy changes during the adsorption and desorption processes.

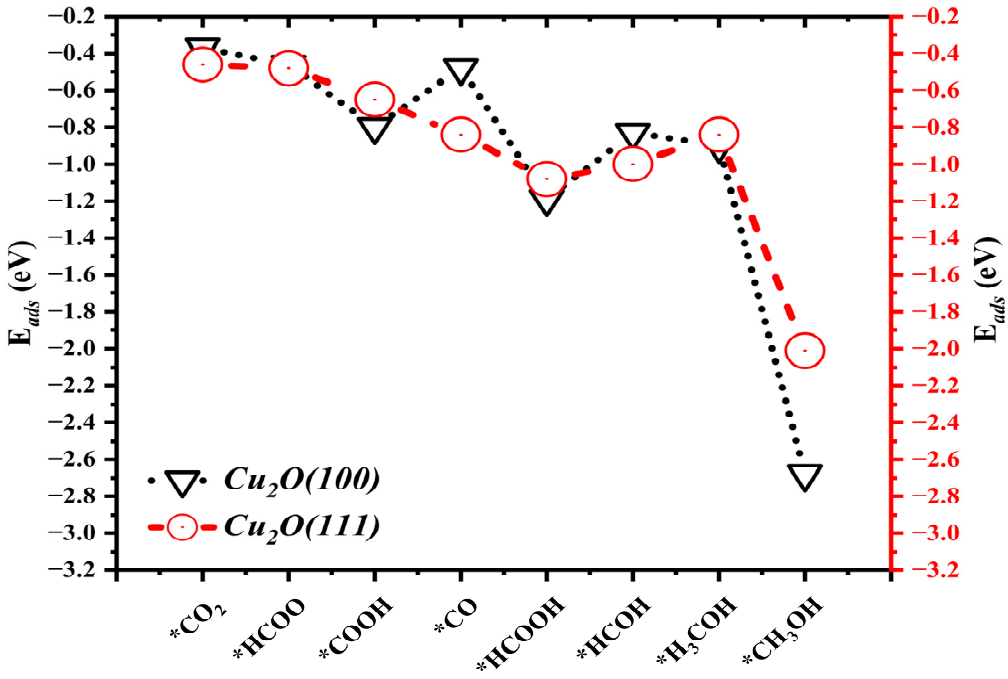


Figure 3. Adsorption energies of different adsorbates on Cu_2O (100) and Cu_2O (111).

The compounds with low molecular weight yielded less negative adsorption. The E_{ads} released during $*CO_2$ was less negative (−0.37 eV) than the E_{ads} of *HCOOH (−1.19 eV) on Cu_2O (100), which indicates that $*CO_2 \rightarrow CO_2$ or CO is more exergonic than $*CO_2 \rightarrow$ HCOOH. The E_{ads} show a good correlation with molecular activation, as discussed in

the previous section. The Cu_2O (111) also documented similar results, where *CO_2 and *HCOOH recorded E_{ads} of −0.46 eV and −1.08 eV, respectively. The E_{ads} for *CH_3OH on Cu_2O (100) and Cu_2O (111) were recorded at −2.8 eV and −2.0 eV, respectively, indicating the bulk adsorption of *CH_3OH on Cu_2O (100) than Cu_2O (111). On the other hand, *CO_2 recorded the lowest E_{ads}, considering it is produced in the first elementary step before hydrogenation. The adsorption energies (E_{ads}) of *CO were found to be −0.48 eV for the (100) surface and a much lower value of −0.84 eV for the (111) surface. The adsorption energy value indicates the stability of the adsorbate on the catalyst surface where a more negative value means a stronger bond and more stable adsorption. In this case, CO molecules have a stronger interaction with Cu_2O (111) than Cu_2O (100). Furthermore, the more negative values of E_{ads} (stronger bond) from CO_2 activation to *CH_3OH can be explained by the increasing number of H and O atoms available in the molecular structures. A slightly higher difference in adsorption energies between *H_3CO and *CH_3OH was observed during the interaction of H from *H_3CO and C/O from *CH_3OH. Moreover, the weak van der Waals forces between hydrogen (H) and copper (Cu) or oxygen (O), combined with the strong chemical bonding of carbon (C) or oxygen (O) to copper, can lead to the formation of $CuCO_3$ or $Cu(OH)_2$. This results in the deactivation of the catalyst surface. Therefore, further investigation of the catalyst surface using bulk electrolysis or long-term chronoamperometric measurements is recommended.

2.3. ΔG Profiles and Reduction Pathways of CO_2ER

The ΔG profiles of the $CO_{(g)}$, $HCOOH_{(l)}$, $HCOH_{(l)}$, and $CH_3OH_{(l)}$ products derived from DFT calculations on both surfaces are given in Figure 4. Based on the results, CO_2 activation energies on Cu_2O (100) and (111) were recorded at −0.37 eV and −0.45 eV, respectively. The data also revealed that *CO_2 reduction to *HCOO is endergonic (non-spontaneous) on both surfaces compared to *COOH. Conversely, the *CO_2 to *COOH reaction is slightly negative and exergonic (spontaneous), with a ΔG of −0.34 eV and −0.20 eV on the Cu_2O (100) and (111) surfaces, respectively.

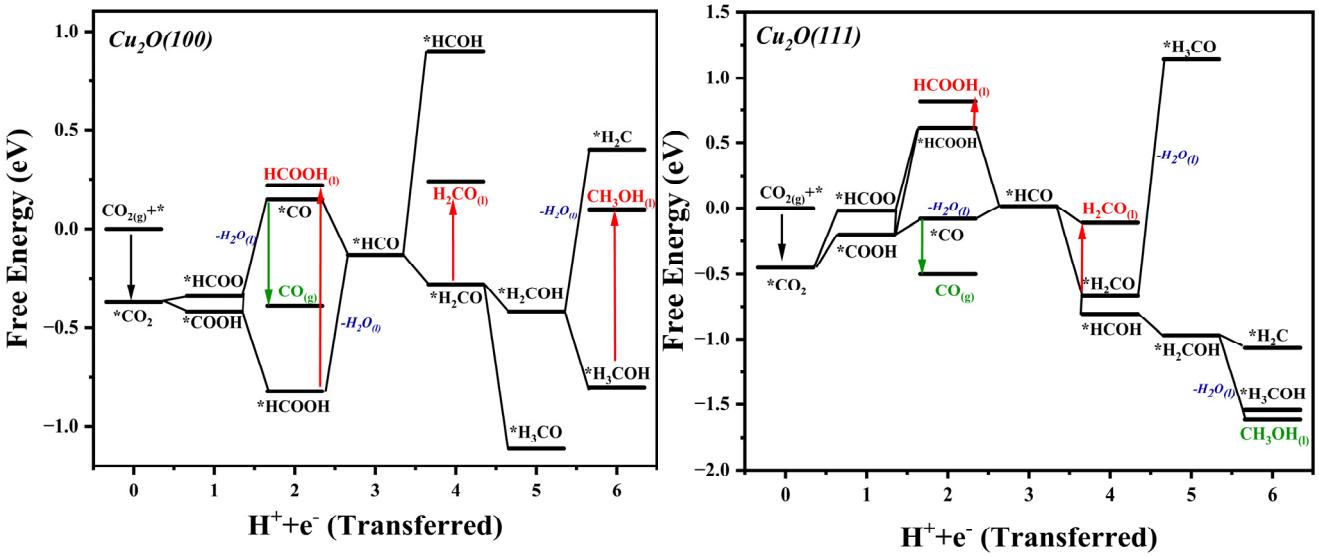


Figure 4. The free energy (ΔG) diagram for various products over Cu_2O (100), and Cu_2O (111) surfaces.

The formation of *HCOOH from *HCOO and *COOH intermediates is exergonic, with a ΔG of −0.82 eV and −0.10 eV for Cu_2O (100) and (111), respectively. The results indicate that *COOH production and desorption are constructive in both facets. Nonetheless, $HCOOH_{(l)}$ desorption needs more energy than $CO_{(g)}$ production. The reaction also origi-

nated at the negative side of the energy profile, confirming $CO_{(g)}$ as the primary product on both surfaces. Consequently, $CO_{(g)}$ production following the $*CO_2 \rightarrow *COOH \rightarrow *HCOOH \rightarrow CO_{(g)}$ pathway is more favourable than the $HCOOH_{(l)}$ pathway, according to the $*CO_2 \rightarrow *COOH \rightarrow *HCOOH \rightarrow HCOOH_{(l)}$ reaction pathway.

An experimental report also supported the findings in this study that $CO_{(g)}$ production was more quantitative in primary reactions [71]. It can be proved that the $*CO_2 \rightarrow *COOH \rightarrow *HCOOH$ reaction is more spontaneous than $*CO_2 \rightarrow *HCOO \rightarrow *HCOOH$. The energy differences calculated for $HCOH_{(l)}$ desorption for the two pathways $*CO_2 \rightarrow *HCOO \rightarrow *CO \rightarrow *HCO \rightarrow *H_2CO \rightarrow HCOH_{(l)}$ and $*CO_2 \rightarrow *COOH \rightarrow *HCOOH \rightarrow *HCO \rightarrow *H_2CO \rightarrow H_2CO_{(l)}$, were −0.72 eV and −1.77 eV, respectively. Based on the results, the $*CO_2 \rightarrow *COOH$ pathway is more exergonic than $*CO_2 \rightarrow *HCOO$ for $HCOH_{(l)}$ production on Cu_2O (100). Similarly, concerning the pathways from *HCOH onwards, the $*HCOH \rightarrow *H_3CO \rightarrow *H_3COH \rightarrow CH_3OH_{(l)}$ reaction is more favourable than the $*HCOH \rightarrow *H_2COH \rightarrow *H_3COH \rightarrow CH_3OH_{(l)}$ counterpart to yield $CH_3OH_{(l)}$. The reaction pathways and changes in the reaction ΔG for all elementary steps are listed in Table 2.

Table 2. The changes in the reaction ΔG for all elementary steps on Cu_2O (100) and Cu_2O (111).

Reaction	ΔG (eV) for Cu_2O (100)	ΔG (eV) for Cu_2O (111)
$* + CO_2(g) \rightarrow *CO_2$	−0.37	−0.11
$*CO_2 \rightarrow *HCOO$	0.22	−0.12
$*CO_2 \rightarrow *COOH$	0.30	0.08
$*HCOO \rightarrow *CO + H_2O$	−0.10	0.16
$*COOH \rightarrow *CO + H_2O$	−0.43	0.43
$*COOH \rightarrow *HCOOH$	0.27	0.50
$*CO \rightarrow *HCO$	−0.14	0.23
$*HCO \rightarrow *HCOH$	0.14	0.41
$*HCO \rightarrow *H_2CO$	0.003	0.29
$*HCO \rightarrow *H_2COH$	0.05	0.46
$*HCO \rightarrow *H_3CO$	0.86	0.63
$*H_2COH \rightarrow *H_2C + H_2O$	0.37	−0.05
$*H_2COH \rightarrow *H_3COH$	0.60	0.45
$*H_3COH \rightarrow CH_3OH$	0.07	0.08

It can then be deduced that the surface of the Cu_2O (111) shows higher exposure to O atoms than C atoms compared to those of the Cu_2O (100) surfaces during its crystallographic oxygen orientation, which enhances the chances of hydrogenation to proceed further and form CH_3OH. Consequently, the two surfaces show different energy profiles. At a laboratory scale, the crystallographic planes of Cu_2O (100) and (111) can be synthesized via wet chemical reductions, electrodeposition, anodization, and solvothermal synthesis [45], and can be used as electrocatalysts for CO_2ER. The products, such as $H_2CO_{(l)}$ from $*H_2CO$ or $*H_2COH$, and $CO_{(g)}$ from *CO, obtained with Cu_2O (100), were slightly more spontaneous than Cu_2O (111). Nevertheless, among the CO_2 reduction to CH_3OH pathways evaluated in this study, the $*CO_2 \rightarrow *COOH \rightarrow *HCOOH \rightarrow *HCO \rightarrow *HCOH \rightarrow *H_2COH \rightarrow *H_3COH \rightarrow CH_3OH_{(l)}$ reaction with Cu_2O (111) shows the shortest pathway, as shown in Figure 5. The reaction involving Cu_2O (100) required an additional 0.90 eV to produce CH_3OH, determined from $*H_3COH$ adsorption according to DFT energy calculations and ZPE profiles.

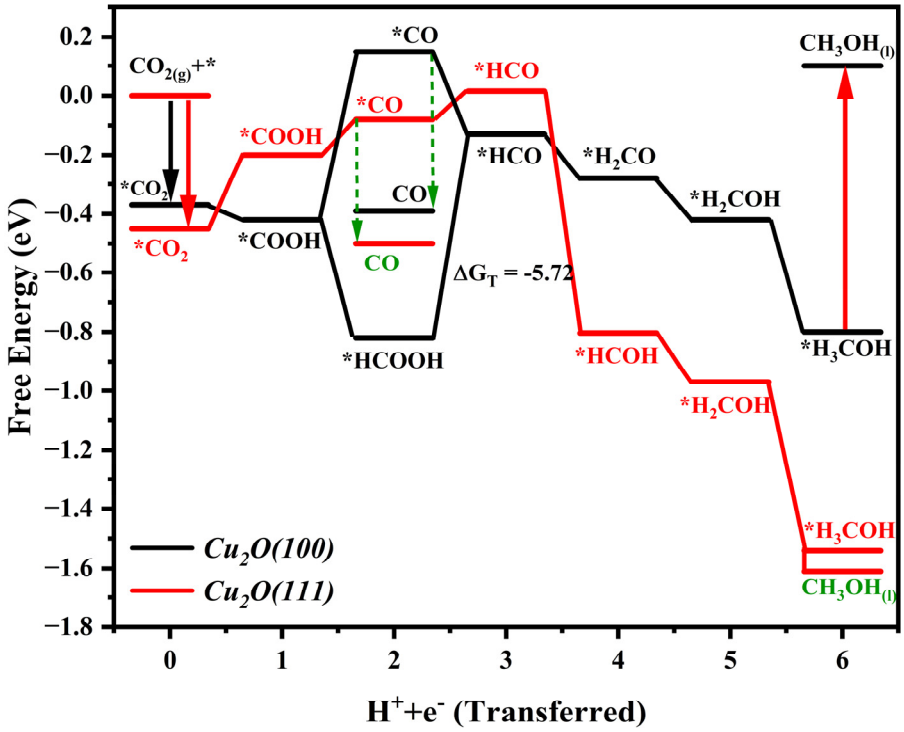


Figure 5. The two different pathways for CO_2ER to CH_3OH over the Cu_2O (100) and Cu_2O (111) surfaces.

The (100) surfaces exhibited energy profiles closer to positive values, with minor deviations in adsorbates. In contrast, the Cu_2O (111) surface remained on the negative side of the energy profile, showing a more significant energy difference from *HCOOH to *HCO compared to the Cu_2O (100) facet. This shows that the Cu_2O (111) surface has higher catalytic activity and reaction rates. Based on calculations, the total ΔG needed to reduce $*CO_2$ to CH_3OH with Cu_2O (100) and (111) was approximately −3.14 eV and −5.72 eV, respectively. Negative values of ΔG indicate that the reaction is spontaneous and energetically favourable. Consequently, this makes the Cu_2O (111) surface a more viable choice for the electroreduction of CO_2 to CH_3OH.

Detailed reactions are documented in Supplementary Materials Equations (S9)–(S21), while the direct conversion of adsorbate from its latest reaction coordinates and possible reduction pathways are illustrated in Figure 6. $*CO_2$ is adsorbed on the surface and proceeded towards $CH_3OH_{(l)}$ with multiple electron–proton transfer via hydrogenation. The $CO_{(g)}$ in this case can be produced from adsorbed *HCOO or *COOH, which remain adsorbed on the catalyst surface and are then converted into *HCOOH via hydrogenation, where $HCOOH_{(l)}$ is easily produced. The *HCO generated after the removal of the hydroxide anions is converted into $H_2CO_{(l)}$ or *HCOH which can then proceed to produce CH_3OH and CH_4. Understanding the energy pathways for these products can help predict the applied potential needed at the laboratory scale for feasible CO_2ER into value-added products. Based on the elementary phases and activation energies, the ΔG for the catalyst Cu_2O (100), in descending, order are: $*H_3CO$ < $*H_3COH$ < $*H_2C$ < *COOH < *HCOOH < *HCOH < $*CH_3OH$(l) < $*H_2COH$ < $*H_2CO$ < *CO < *HCO < $*CO_2$. Meanwhile, the ΔG for the catalyst Cu_2O (111) are: $*H_3CO$ < *HCOOH < $*H_2COH$< $*H_3COH$ < *CO < *HCO < $*H_2CO$ < *HCOH < *COOH < $*CH_3OH$(l) < $*H_2C$ < *HCOO < $*CO_2$.

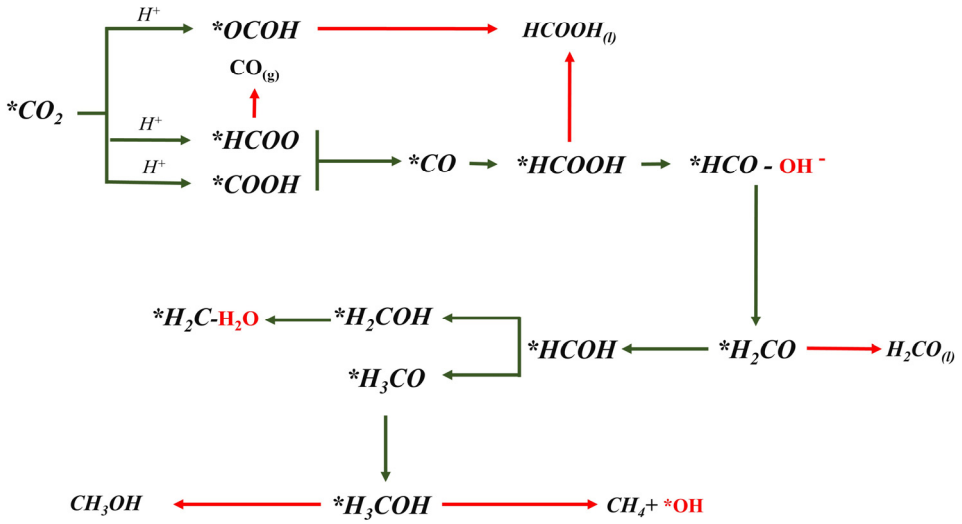


Figure 6. The suggested CO_2 reduction pathways to $CO_{(g)}$, $HCOOH_{(l)}$, $H_2CO_{(l)}$, and CH_3OH. The red arrows indicate the desorption pathways for different products.

The data showed that $*H_3CO$ interactions consumed the most energy, while $*CO_2$ interactions required the least energy in both cuprous oxides. The total energy required to reduce $*CO_2$ to *CO through the *COOH pathway is -0.5 eV employing Cu_2O (100), while Cu_2O (111) recorded a value of 0.4 eV. The results indicated that Cu_2O (100) is superior to Cu_2O (111) for $CO_{(g)}$ and bicarbonate production. Nonetheless, the oxide is unsuitable for transforming $CO_{(g)}$ to $CH_3OH_{(l)}$ due to the higher potential required.

The formation of CH_3OH exhibits sluggish reaction rates, as it involves six electron transfers through various intermediates. In contrast, products such as formate or CO require less electron transfer and have higher reaction rates. Additionally, catalysts tend to decline in activity over time, further reducing reaction rates. Our results demonstrate that the extensive pathway for CH_3OH formation leads to low reaction rates from $*CO_2$ to CH_3OH (Figures 5 and 6).

These reaction pathways suggest that CO_2ER to CH_3OH needs a longer reaction pathway requiring higher overpotentials than formate or CO. Consequently, based on our findings, the Cu_2O (100) surface is not effective for long reactions due to surface reconstruction, unlike the more stable Cu_2O (111) (Figure 2a). Nonetheless, doping or complexing Cu_2O with single-atom catalysts (SACs) could enhance reaction stability and increase reaction rates for CH_3OH formation, as supported by previous reports [72–76].

On the other hand, a straightforward and favourable reaction pathway from CO_2 to CH_3OH is proposed using Equations (6)–(9). In this pathway, an oxygen atom from either the Cu_2O (100) or Cu_2O (111) surface adsorbs onto the carbon atom of CO_2, forming a carboxyl (COOH) radical. This radical then reacts with hydrogen/protons to produce formic acid (HCOOH). As previously discussed, the carbon atom in formic acid has a higher affinity for the Cu_2O (111) surface, especially when an exposed oxygen atom is present. This interaction promotes the formation of methanol (CH_3OH).

$$CO_2 + e^- \rightarrow CO_2^* \quad (6)$$

$$CO_2^* + H^+ \rightarrow COOH \quad (7)$$

$$COOH + e^- + H^+ \rightarrow H^*COOH \quad (8)$$

$$H^*COOH + e^- + H^+ \rightarrow CH_3OH \quad (9)$$

According to the results presented in this work, CO desorption from *HCOO is achievable by applying extra potential, following the trends of energy activation. This process breaks the C-O bonds, converting *HCOO to CO from metal oxide sites. Alternatively, *COOH will lead to *CO production via O-H removal in the form of water. *OCHO production on metal sites is also possible from oxide formation. Initially, metals are converted to metal oxides, which can directly produce $HCOOH_{(l)}$. Cu_2O, being a metal oxide, provides the highest yield of $HCOOH_{(l)}$ [77]. $H_2CO_{(l)}$ can be obtained through a four-electron reduction process: $*HCOOH \rightarrow *HCO + H_2O \rightarrow *H_2CO \rightarrow H_2CO_{(l)}$. Similarly, sequential protonation of $*HCOOH \rightarrow *HCO + H_2O \rightarrow *H_2CO \rightarrow *H_3CO \rightarrow *H_3COH \rightarrow CH_3OH_{(l)}$ produces $CH_3OH_{(l)}$. However, these pathways depend on the relative hydrogenation stability of the catalyst [78,79].

Several studies have verified the synthesis of the octahedron (111), hexagonal (111), and dodecahedral (110) crystal facets with six, eight, and twelve crystal planes from cubic Cu_2O (100) through X-ray diffraction (XRD) analysis [80,81]. Although most reports focused on performance without considering the effects on electronic energies, the free energy values documented in this study are comparable with other reported computational studies as shown in Table 3.

Table 3. Comparison of free energies calculated for cuprous oxide (Cu_2O) using DFT.

Adsorbate	Adsorbent	Free Energy (eV)	Reference
$*CO_2$	Cu_2O (100) Cu_2O (111)	−0.37 −0.11	This work
*HCOO	Cu_2O (100) Cu_2O (111)	0.22 −0.12	This work
*COOH	Cu_2O (100) Cu_2O (111)	0.30 0.08	This work
*CO	Cu_2O (111) Cu_2O (100)	−0.10 0.16	This work
*HCOOH	Cu_2O (111) Cu_2O (100)	0.27 0.50	This work
$*CO_2$ *HCOO *COOH *CO *HCOOH	Cu_2O (111)	−0.09 −0.14 0.35 −0.50 −0.40	[82]
CO_2 *CO *HCOOH	Cu_2O (111)	0.00 −0.50 −0.01	[83]
$*CO_2$ *COOH *CO	Cu_2O (111)	−0.13 −0.12 −0.65	[84]
CO_2 COOH CO HCOOH	Cu_2O	0.00 0.10 −1.00 −0.50	[85]

Furthermore, the correlation of the respective energies offers various avenues for material selection. For example, nanosized Cu_2O particles were developed and enclosed within cubic Cu_2O (100) and Cu_2O (111) octahedron structures utilizing the hydrothermal method [86]. The study reported 35.4% as the highest FE, achieved with the octahedron Cu_2O (111) structure, while 26.2% FE was achieved by the cubic Cu_2O (100) for alcohol

base products [86]. In another study, CO_2 was reduced to methane with 66.57% FE on the exposed surfaces of Cu nanostructure with predominant (111) orientation [87]. A facet-regulating experiment yielded Cu_2O (111) nanocatalysts. The substance was produced via the reductant-controlled method and achieved 74.1% FE for ethylene (C_2H_4) [88]. Performance comparison of various products between Cu_2O (100) and Cu_2O (111) from different literatures is presented in Table 4.

Table 4. CO_2ER products and performance over cuprous oxide (Cu_2O).

Material	Product	% Faradic Efficiency	References
Cu_2O (100)	CH_3OH	26.20	[86]
Cu_2O (111)	CH_3OH	35.7	
Cu_2O (100)	CO	20	
Cu_2O (111)	CO	40	
Cu_2O (100)	C_2H_4	38	[45]
Cu_2O (111)	C_2H_4	45	
Cu_2O (111)	CH_3OH	29.1	[89]
Cu_2O (100)	C_2H_4	30.1	[90]
Cu_2O (111)	C_2H_4	44.9	
Cu_2O (111)/Cu_2O (100)	C_2H_4	57.8	

Research on the same material found that the tetrahedral Cu_2O (111) crystal lattice was favourable for CH_3OH selectivity when modified from Cu_2O (100). Other studies indicated that the highest $CO_{(g)}$ FE was achieved with cubic Cu_2O (100) [91,92], supporting the findings of this study. The literature also noted that CH_3OH production with Cu_2O (111) was optimal due to its defect-free nature, which offers more adsorption sites and surface oxygen availability. At 140 K, the surfaces could form a mixed layer of methoxy, formaldehyde, and other CH-containing species [93]. The active CH-bond breaking properties of the structure also enable the catalyst to convert CO_2 to CH_3OH [94]. Conclusively, the surface of Cu_2O (111) possesses exceptional structural and electrical characteristics, making it efficient for the selective electrochemical reduction of CO_2 to CH_3OH [93]. These attributes include the availability of adsorption sites, surface oxygen, and the capacity to stimulate crucial reaction steps. Additionally, doping other elements with different orientations and ratios on copper and copper oxides could lead to varied results [95].

3. Model and Computational Details

The DFT calculations in the current study were performed using the DMol^3 in Materials Studio (MS 20.1). The selection of DFT calculations, utilizing a transition from a single crystal to an amorphous system, aligns well with the parameters employed in this study. DFT has been widely reported in numerous research studies for its high quality and accuracy, particularly when analysing different molecules across a broad range of crystal systems [96–98]. The evaluations were conducted in a generalized gradient approximation (GGA) as an exchange-correlation function according to the Perdew–Burke–Ernzerh (PBE) scheme. The calculations were performed on (3 × 3 × 3) Cu_2O (100) and Cu_2O (111) surfaces, a 3.71 Å lattice constant, a 2 × 3 surface slab, and a 20 Å thick vacuum slab perpendicular *z*-direction to avoid periodic interaction between periodic images.

The vacuum slab was constructed consisting of three atomic layers, where the top layer of Cu_2O was kept relaxed during geometry optimization and the bottom two layers were kept fixed. For all intermediate adsorptions, a top hollow site with perpendicular orientation was consistently employed as the model configuration. The intermediates and stable compounds were placed between hollow sites of Cu and O to see the possible

interaction of molecules towards catalyst sites. To observe potential interactions between the π-electrons of various adsorbates with the d-orbitals of Cu atoms, and coordination of oxygen lone pairs with Cu sites, a perpendicular orientation was selected. This configuration provides multiple Cu atoms for coordination, promoting the stabilization of intermediates through chemical bonding. Furthermore, the presence of surface oxygen atoms on Cu_2O can contribute to hydrogen bonding or polar interactions, potentially facilitating the hydrogenation pathway.

In this study, the spin moment under regular crystals was restricted, while geometry optimization for free molecules was marked as unrestricted. Ideal unit cells were obtained by employing cartesian coordinates. In the present study, all electrons were selected for core treatment. A double numerical plus d-functions (DND) numerical basis set at a 4.4 basis file was employed due to significant atomic mass. The gamma k-point set was used during electronic calculations, which aided orbital determinations. Geometry optimization in this study was performed at the lowest observed binding energy.

According to the CHE model, the standard hydrogen electrode (SHE) is used to measure the redox potential, which is based on reversible hydrogen redox reaction and can be written as Equations (10) and (11) [99].

$$H_2 \rightarrow 2H^+ + 2e^- \tag{10}$$

$$H^+_{(aq)} + e^- \leftrightharpoons \frac{1}{2}H_{2(g)} \tag{11}$$

The electrode potential in this relation is computed by subtracting the experimental value of the absolute standard hydrogen electrode potential from the calculated potential of any other reference electrode potential. On the contrary, if the SHE itself is used as a reference electrode, then the potential of this SHE is added to the value of the working electrode and species reacting with that electrode. Hence, following the same calculations, the free energy values for all intermediates determined through DFT were added from the hydrogen energies relevant to the balanced e reactions in this study (given in Supplementary Materials from Equations (S9)–(S21)). The oxidation–reduction in the current study was determined according to Equations (12)–(14):

$$\frac{1}{2}O_2 + * \rightarrow O^* \tag{12}$$

$$O^* + H^+ + e^- \rightarrow HO^* \tag{13}$$

$$HO^* + H^+ + e^- \rightarrow H_2O + * \tag{14}$$

where * denotes the catalyst site.

The same method was used for all adsorbates and intermediates adsorption and activation on Cu_2O surfaces having different facets. The SHE was employed to compare catalyst sites and various species participating in CO_2 activation to CH_3OH desorption post-foundation. For all reaction coordinates, the parameters employed for the calculation were based on $H^+ + e^-$ transfer at standard potential (pH 7, 1 bar pressure, and 298 K temperature) as given in Equations (8)–(10). The free energy of hydrogen was first optimized using DFT and used for further calculations, including free energy profiles and adsorption energies (E_{ads}).

E_{ads} were determined following Equation (15). The Gibbs free energy (ΔG) of all elementary steps involved was computed utilizing chemical reactions based on ($H^+ + e^-$)

transfer on the adsorbed CO_2 hydrogenation. A detailed reaction adsorption energy list for all species is presented in Supplementary Information Equations (S1)–(S8) [54]:

$$E_{ads} = E_{slab+ads}^{total} - E_{iso-slab} - E_{iso-ads} \quad (15)$$

where *slab* represents the unit cells with Cu_2O (100) and Cu_2O (111) catalysts, *iso-slab* denotes the isolated slab system, and *ads* indicates adsorption.

4. Conclusions

In this study, density functional theory (DFT) calculations were employed to predict and understand the electrocatalytic properties of CO_2 electroreduction (CO_2ER) to C_1 products over Cu_2O (100) and Cu_2O (111) catalysts using the computational hydrogen electrode (CHE) model. The study focused on the performance of CO_2ER towards CH_3OH production on different facets of Cu_2O. The results showed that carbon monoxide (CO) formation was favoured during the initial reduction of CO_2 on both crystallographic planes. However, the Cu_2O (111) surface, with its protrusions, exhibited higher catalytic activity and selectivity for methanol ($CH_)$ compared to Cu_2O (100). The production of CH_3OH on Cu_2O (111) was more exergonic than on Cu_2O (100). Both Cu_2O (100) and Cu_2O (111) surfaces demonstrated similar tendencies to produce CO at low potentials during the decoupling of carbon from adsorbed $*CO_2$. Theoretically, the small Cu_2O cubic structure has a higher active surface area for CO selectivity than cupric oxide (CuO) and demonstrated stability in catalysis during CO production. These findings are consistent with data reported in other studies. The study demonstrated that crystallographic orientation affects adsorbates and desorption paths in CO_2ER. The analysis of the free energies of adsorption and desorption indicated that the reaction proceeded through CO_2 activation, leading to the formation of CH_3OH. This computational approach can help screen potential electrocatalysts and understand reaction pathways to achieve desired value-added products like CH_3OH. Further experimental validation at the laboratory scale is essential to confirm these findings.

Supplementary Materials: The following supporting information can be downloaded at: https://www.mdpi.com/article/10.3390/catal15020130/s1, Table S1: Change in angles in O-Cu-O and Cu-O-Cu in Cu_2O (100) and Cu_2O (111) after interaction of different adsorbents; Table S2: E_{ads} calculated for Cu_2O (100) and Cu_2O (111); Equations (S1)–(S8) used to calculate E_{ads} of various adsorbates; Equations (S9)–(S21): All chemical reactions of different species for adsorption; Table S3: The standard thermodynamic quantities of different species, molecules, and catalysts calculated at 298 k for Cu_2O (100); Table S4: The standard thermodynamic quantities of different species, molecules, and catalysts calculated at 298 k for Cu_2O (111). Ref. [100] is cited in the Supplementary Materials.

Author Contributions: Z.A.L.: Original manuscript write-up, and performed simulations and data analysis. W.Z.N.Y.: conceptualization, supervision, writing, review and editing, formal analysis, proofreading, project administration, and funding acquisition. S.A.S.M.: review and editing, formal analysis, and proofreading. M.A.B.: supervision and resources. All authors have read and agreed to the published version of the manuscript.

Funding: The authors also wish to express their thanks for the financial support provided by the YUTP-FRG (015LC0-455) grant.

Data Availability Statement: The data supporting this article have been included in the Supplementary Materials. The computational data and materials used in this paper are available upon request.

Acknowledgments: The authors would like to express gratitude to the Department of Chemical Engineering and the Centre of Research in Ionic Liquids (CORIL) of Universiti Teknologi PETRONAS for providing technical assistance and research facilities.

Conflicts of Interest: The authors declare no conflict of interest.

References

1. Kabir, M.; Habiba, U.E.; Khan, W.; Shah, A.; Rahim, S.; Rios-Escalante, P.R.D.l.; Farooqi, Z.-U.-R.; Ali, L.; Shafiq, M. Climate change due to increasing concentration of carbon dioxide and its impacts on environment in 21st century; a mini review. *J. King Saud Univ.-Sci.* **2023**, *35*, 102693. [CrossRef]
2. Yang, M.; Chen, L.; Wang, J.; Msigwa, G.; Osman, A.I.; Fawzy, S.; Rooney, D.W.; Yap, P.-S. Circular economy strategies for combating climate change and other environmental issues. *Environ. Chem. Lett.* **2022**, *21*, 55–80. [CrossRef]
3. Schleussner, C.-F.; Ganti, G.; Rogelj, J.; Gidden, M.J. An emission pathway classification reflecting the Paris Agreement climate objectives. *Commun. Earth Environ.* **2022**, *3*, 135. [CrossRef]
4. Abdul-Latif, N.S.; Ong, M.Y.; Nomanbhay, S.; Salman, B.; Show, P.L. Estimation of carbon dioxide (CO_2) reduction by utilization of algal biomass bioplastic in Malaysia using carbon emission pinch analysis (CEPA). *Bioengineered* **2020**, *11*, 154–164. [CrossRef] [PubMed]
5. Modak, A.; Bhanja, P.; Dutta, S.; Chowdhury, B.; Bhaumik, A. Catalytic reduction of CO_2 into fuels and fine chemicals. *Green Chem.* **2020**, *22*, 4002–4033. [CrossRef]
6. Fouda, A. Nano-porous Carbon-Based Electrodes for the Electrocatalytic Reduction of CO_2 to Methanol. Doctoral Dissertation, Khalifa University of Science, Abu Dhabi, United Arab Emirates, 2023.
7. Lu, S.; Lou, F.; Yu, Z. Recent progress in two-dimensional materials for electrocatalytic CO_2 reduction. *Catalysts* **2022**, *12*, 228. [CrossRef]
8. Albo, J.; Alvarez-Guerra, M.; Castaño, P.; Irabien, A. Towards the electrochemical conversion of carbon dioxide into methanol. *Green Chem.* **2015**, *17*, 2304–2324. [CrossRef]
9. Joghee, P.; Malik, J.N.; Pylypenko, S.; O'Hayre, R. A review on direct methanol fuel cells–In the perspective of energy and sustainability. *MRS Energy Sustain.* **2015**, *2*, E3. [CrossRef]
10. Tabibian, S.S.; Sharifzadeh, M. Statistical and analytical investigation of methanol applications, production technologies, value-chain and economy with a special focus on renewable methanol. *Renew. Sustain. Energy Rev.* **2023**, *179*, 113281. [CrossRef]
11. Panafidin, M.A.; Bukhtiyarov, A.V.; Fedorov, A.Y.; Bukhtiyarova, M.V.; Prosvirin, I.P.; Bukhtiyarov, V.I. In situ XPS study of methanol oxidation over a copper catalyst derived from layered double hydroxides. *Catal. Sci. Technol.* **2024**, *14*, 4986–4996. [CrossRef]
12. Marcandalli, G.; Monteiro, M.C.O.; Goyal, A.; Koper, M.T.M. Electrolyte Effects on CO_2 Electrochemical Reduction to CO. *Acc Chem. Res.* **2022**, *55*, 1900–1911. [CrossRef]
13. Kumar, A.; Aeshala, L.M.; Palai, T. Electrochemical reduction of CO_2 to useful fuel: Recent advances and prospects. *J. Appl. Electrochem.* **2023**, *53*, 1295–1319. [CrossRef]
14. Razzaq, A.; In, S.-I. TiO_2 based nanostructures for photocatalytic CO_2 conversion to valuable chemicals. *Micromachines* **2019**, *10*, 326. [CrossRef] [PubMed]
15. Kiendl, B. Application of Diamond Nanomaterials in Catalysis. Doctoral Dissertation, Universität Würzburg, Würzburg, Germany, 2020.
16. Siwek, H.; Łukaszewski, M.; Czerwiński, A. Electrochemical study on the adsorption of carbon oxides and oxidation of their adsorption products on platinum group metals and alloys. *Phys. Chem. Chem. Phys.* **2008**, *10*, 3752–3765. [CrossRef] [PubMed]
17. Lee, M.-Y.; Park, K.T.; Lee, W.; Lim, H.; Kwon, Y.; Kang, S. Current achievements and the future direction of electrochemical CO_2 reduction: A short review. *Crit. Rev. Environ. Sci. Technol.* **2020**, *50*, 769–815. [CrossRef]
18. Hussain, I.; Alasiri, H.; Ullah Khan, W.; Alhooshani, K. Advanced electrocatalytic technologies for conversion of carbon dioxide into methanol by electrochemical reduction: Recent progress and future perspectives. *Coord. Chem. Rev.* **2023**, *482*, 215081. [CrossRef]
19. Ait Ahsaine, H.; BaQais, A. Metal and metal oxide electrocatalysts for the electrochemical reduction of CO_2-to-C1 chemicals: Are we there yet? *Green Chem. Lett. Rev.* **2023**, *16*, 2160215. [CrossRef]
20. An, X.; Wang, P.; Ma, X.; Du, X.; Hao, X.; Yang, Z.; Guan, G. Application of ionic liquids in CO_2 capture and electrochemical reduction: A review. *Carbon Resour. Convers.* **2023**, *6*, 85–97. [CrossRef]
21. Alsunni, Y.A.; Alherz, A.W.; Musgrave, C.B. Electrocatalytic reduction of CO_2 to CO over Ag (110) and Cu (211) modeled by grand-canonical density functional theory. *J. Phys. Chem. C* **2021**, *125*, 23773–23783. [CrossRef]
22. Guzmán, H.; Russo, N.; Hernández, S. CO_2 valorisation towards alcohols by Cu-based electrocatalysts: Challenges and perspectives. *Green Chem.* **2021**, *23*, 1896–1920. [CrossRef]

23. Alamro, F.S.; Medany, S.S.; Al-Kadhi, N.S.; Mostafa, A.M.; Zaher, W.F.; Ahmed, H.A.; Hefnawy, M.A. Controllable Synthesis of Fe_2O_3/Nickel Cobaltite Electrocatalyst to Enhance Oxidation of Small Molecules. *Catalysts* **2024**, *14*, 329. [CrossRef]
24. Shi, H.; Wu, L.; Zhang, Q.; Zhang, Y.; Sun, W.; Liu, C.; Zhang, R. Preparation and Electrocatalytic Properties of One-Dimensional Nanorod-Shaped N, S Co-Doped Bimetallic Catalysts of FeCuS-N-C. *Catalysts* **2024**, *14*, 849. [CrossRef]
25. Wang, Y.; Zheng, M.; Wang, X.; Zhou, X. Electrocatalytic Reduction of CO_2 to C1 Compounds by Zn-Based Monatomic Alloys: A DFT Calculation. *Catalysts* **2022**, *12*, 1617. [CrossRef]
26. Yun, G.; Young Hwang, S.; Young Kim, S.; Gwon, Y.; Bae, S.; Kyun Rhee, C.; Sohn, Y. Exploring Pd-Ag/Cu electrodes in electrochemical CO_2 reduction: Insights into C1, C2, and C3+ chemistry. *Appl. Surf. Sci.* **2024**, *665*, 160279. [CrossRef]
27. Jia, S.; Wu, L.; Xu, L.; Sun, X.; Han, B. Multicomponent catalyst design for $CO_2/N_2/NOx$ electroreduction. *Ind. Chem. Mater.* **2023**, *1*, 93–105. [CrossRef]
28. Roy, A.; Jadhav, H.S.; Gil Seo, J. Cu_2O/CuO Electrocatalyst for Electrochemical Reduction of Carbon Dioxide to Methanol. *Electroanalysis* **2020**, *33*, 705–712. [CrossRef]
29. Wang, P.; Yang, H.; Tang, C.; Wu, Y.; Zheng, Y.; Cheng, T.; Davey, K.; Huang, X.; Qiao, S.Z. Boosting electrocatalytic CO_2-to-ethanol production via asymmetric C-C coupling. *Nat Commun.* **2022**, *13*, 3754. [CrossRef]
30. Ouyang, Y.; Shi, L.; Bai, X.; Li, Q.; Wang, J. Breaking scaling relations for efficient CO_2 electrochemical reduction through dual-atom catalysts. *Chem. Sci.* **2020**, *11*, 1807–1813. [CrossRef]
31. Yun, G.; Hwang, S.Y.; Maeng, J.Y.; Kim, Y.J.; Rhee, C.K.; Sohn, Y. Electrochemical CO_2/CO reduction on Ag/Cu electrodes and exploring minor Fischer–Tropsch reaction pathways. *Appl. Surf. Sci.* **2024**, *649*, 159179. [CrossRef]
32. Liu, Y.; Li, F.; Zhang, X.; Ji, X. Recent progress on electrochemical reduction of CO_2 to methanol. *Curr. Opin. Green Sustain. Chem.* **2020**, *23*, 10–17. [CrossRef]
33. Darban, M.A.; Lock, S.S.M.; Ilyas, S.U.; Kang, D.Y.; Othman, M.H.D.; Yiin, C.L.; Waqas, S.; Bashir, Z. Molecular simulation of [P8883][Tf(2)N] ionic liquid decorated silica in 6FDA-ODA based mixed matrix membrane for enhanced CO_2/CH_4 separation. *RSC Adv.* **2024**, *14*, 22894–22915. [CrossRef] [PubMed]
34. Cheng, Y.; Xu, X.; Li, Y.; Zhang, Y.; Song, Y. CO_2 reduction mechanism on the Nb2CO_2 MXene surface: Effect of nonmetal and metal modification. *Comput. Mater. Sci.* **2022**, *202*, 110971. [CrossRef]
35. Mohammed, S.A.S.; Yahya, W.Z.N.; Bustam, M.A. Computational studies of ionic liquids as co-catalyst for CO_2 electrochemical reduction to produce syngas using COSMO-RS. *E3S Web Conf.* **2021**, *287*, 02016. [CrossRef]
36. Almajed, H. *A Theoretical Study of the Electrochemical CO_2 Reduction over Single Atom Catalysts Using Grand-Canonical DFT*; University of Colorado at Boulder: Boulder, CO, USA, 2021.
37. Kuo, T.-C.; Chou, J.-W.; Shen, M.-H.; Hong, Z.-S.; Chao, T.-H.; Lu, Q.; Cheng, M.-J. First-principles study of C–C coupling pathways for CO_2 electrochemical reduction catalyzed by Cu (110). *J. Phys. Chem. C* **2021**, *125*, 2464–2476. [CrossRef]
38. Bi, X.; Yan, Y.; Wang, H.; Zhao, Y.; Zhang, J.; Wu, M. Electroreduction of CO_2 to C_2H_4 Regulated by Spacing Effect: Mechanistic Insights from DFT Studies. *Energy Mater. Adv.* **2023**, *4*, 0037. [CrossRef]
39. Li, C.W.; Kanan, M.W. CO_2 reduction at low overpotential on Cu electrodes resulting from the reduction of thick Cu_2O films. *J. Am. Chem. Soc.* **2012**, *134*, 7231–7234. [CrossRef] [PubMed]
40. Guan, Y.; Suo, W.; Zhang, Z.; Wang, Y.; Sun, S.; Liu, G. Insights on the catalytic active site for CO_2 reduction on copper-based catalyst: A DFT study. *Mol. Catal.* **2021**, *511*, 111725. [CrossRef]
41. Xiao, Y.; Tang, L.; Zhang, W.; Shen, C. Theoretical insights into the selective and activity of CuAu catalyst for O_2 and CO_2 electroreduction. *Comput. Mater. Sci.* **2021**, *192*, 110402. [CrossRef]
42. Chu, S.; Kang, C.; Park, W.; Han, Y.; Hong, S.; Hao, L.; Zhang, H.; Lo, T.W.B.; Robertson, A.W.; Jung, Y. Single atom and defect engineering of CuO for efficient electrochemical reduction of CO_2 to C_2H_4. *SmartMat* **2022**, *3*, 194–205. [CrossRef]
43. Liu, T.; Song, G.; Liu, X.; Chen, Z.; Shen, Y.; Wang, Q.; Peng, Z.; Wang, G. Insights into the mechanism in electrochemical CO_2 reduction over single-atom copper alloy catalysts: A DFT study. *Iscience* **2023**, *26*, 107953. [CrossRef]
44. Masood, Z.; Ge, Q. Electrochemical reduction of CO_2 at the earth-abundant transition metal-oxides/copper interfaces. *Catal. Today* **2023**, *409*, 53–62. [CrossRef]
45. Gao, Y.; Wu, Q.; Liang, X.; Wang, Z.; Zheng, Z.; Wang, P.; Liu, Y.; Dai, Y.; Whangbo, M.H.; Huang, B. Cu_2O Nanoparticles with Both 100 and 111 Facets for Enhancing the Selectivity and Activity of CO_2 Electroreduction to Ethylene. *Adv. Sci.* **2020**, *7*, 1902820. [CrossRef]
46. Haouas, H.; El Atouani, L.; Sbiaai, K.; Hasnaoui, A. Size and temperature effects on surface energy of Au and Fe nanoparticles from atomistic simulations. *Comput. Mater. Sci.* **2022**, *214*, 111695. [CrossRef]
47. Gholizadeh, R.; Pavlin, M.; Huš, M.; Likozar, B. Multiscale Modeling of CO_2 Electrochemical Reduction on Copper Electrocatalysts: A Review of Advancements, Challenges, and Future Directions. *ChemSusChem* **2024**, *18*, e202400898. [CrossRef]
48. Chang, K.; Zhang, H.; Chen, J.G.; Lu, Q.; Cheng, M.-J. Constant Electrode Potential Quantum Mechanical Study of CO_2 Electrochemical Reduction Catalyzed by N-Doped Graphene. *ACS Catal.* **2019**, *9*, 8197–8207. [CrossRef]

49. Masood, Z.; Ge, Q. Comparative Study of Computational Hydrogen Electrodes and Constant Electrode Potential Models Applied to Electrochemical Reduction of CO_2 and Oxygen Evolution Reaction on Metal Oxides/Copper Catalysts. *J. Phys. Chem. C* **2023**, *127*, 23170–23179. [CrossRef]
50. Garza, A.J.; Bell, A.T.; Head-Gordon, M. Mechanism of CO_2 Reduction at Copper Surfaces: Pathways to C2 Products. *ACS Catal.* **2018**, *8*, 1490–1499. [CrossRef]
51. Xue, Y.; Guo, Y.; Cui, H.; Zhou, Z. Catalyst Design for Electrochemical Reduction of CO_2 to Multicarbon Products. *Small Methods* **2021**, *5*, e2100736. [CrossRef]
52. Li, S.; Tong, L.; Peng, Z.; Zhang, B.; Fu, X. Efficient CO_2 reduction for CO production using triatomic catalyst screening: A DFT study. *Appl. Surf. Sci.* **2024**, *644*, 158804. [CrossRef]
53. Wu, R.; Liu, D.; Geng, J.; Bai, H.; Li, F.; Zhou, P.; Pan, H. Electrochemical reduction of CO_2 on single-atom catalysts anchored on N-terminated TiN (1 1 1): Low overpotential and high selectivity. *Appl. Surf. Sci.* **2022**, *602*, 154239. [CrossRef]
54. Kundappaden, I.; Chatanathodi, R. A DFT study of CO adsorption on Pt (111) using van der Waals functionals. *Surf. Sci.* **2019**, *681*, 143–148. [CrossRef]
55. Yang, Y.B.; Hao, Q.; Muller-Plathe, F.; Bohm, M.C. Monte Carlo simulations of SO_2, H_2S, and CO_2 adsorption in charged single-walled carbon nanotube arrays. *J. Phys. Chem. C* **2020**, *124*, 5838–5852. [CrossRef]
56. Jain, A.; Ong, S.; Hautier, G. Commentary: The materials project: A materials genome approach to accelerating materials. *APL Mater.* **2013**, *1*, 011002. [CrossRef]
57. Gražulis, S.; Chateigner, D.; Downs, R.T.; Yokochi, A.; Quirós, M.; Lutterotti, L.; Manakova, E.; Butkus, J.; Moeck, P.; Le Bail, A. Crystallography Open Database–an open-access collection of crystal structures. *J. Appl. Crystallogr.* **2009**, *42*, 726–729. [CrossRef]
58. Coordinators, N.R. Database resources of the national center for biotechnology information. *Nucleic Acids Res.* **2018**, *46*, D8. [CrossRef]
59. Bae, G.-T. *Computational Studies of the Properties of Copper Oxide Clusters and the Reactions of Phenol and Chlorinated Phenols with Copper Oxide Clusters*; Louisiana State University and Agricultural & Mechanical College: Baton Rouge, LA, USA, 2009.
60. Yadav, T.P.; Kaphle, G.C.; Srivastava, A. Computational Study of the Structural, Electronic and Magnetic Properties of Nanoclusters of Cu_2O and CuO: Ab-Initio Approach. *J. Nepal Phys. Soc.* **2020**, *6*, 68–72. [CrossRef]
61. Wang, C.; Tissot, H.; Escudero, C.; Pérez-Dieste, V.; Stacchiola, D.; Weissenrieder, J. Redox properties of Cu_2O (100) and (111) surfaces. *J. Phys. Chem. C* **2018**, *122*, 28684–28691. [CrossRef]
62. Gloystein, A.; Nilius, N.; Goniakowski, J.; Noguera, C. Nanopyramidal reconstruction of Cu_2O (111): A long-standing surface puzzle solved by STM and DFT. *J. Phys. Chem. C* **2020**, *124*, 26937–26943. [CrossRef]
63. Li, G.; Yu, X.; Weststrate, C.; Ren, P.; Xu, J.; Xu, Q.; Yang, Y.; Li, Y.; Niemantsverdriet, J.; Wen, X. Role of Interfaces in the Thermal Reduction Process of the FeO/Cu_2O/Cu (100) Surface. *J. Phys. Chem. C* **2021**, *125*, 20863–20869. [CrossRef]
64. Cheng, T.-K.; Jeromiyas, N.; Lin, Y.-K.; Yang, C.-C.; Kao, C.-L.; Chen, P.-Y.; Lee, C.-L. Spherical and porous Cu_2O nanocages with Cu_2O/$Cu(OH)_2$ Surface: Synthesis and their promising selectivity for catalysing CO_2 electroreduction to C_2H_4. *Appl. Surf. Sci.* **2024**, *660*, 159978. [CrossRef]
65. Sieberer, M.; Redinger, J.; Mohn, P. Electronic and magnetic structure of cuprous oxide Cu_2O doped with Mn, Fe, Co, and Ni: A density-functional theory study. *Phys. Rev. B* **2007**, *75*, 035203. [CrossRef]
66. Li, X.; Chen, Y.; Zhan, X.; Xu, Y.; Hao, L.; Xu, L.; Li, X.; Umer, M.; Tan, X.; Han, B. Strategies for enhancing electrochemical CO_2 reduction to multi-carbon fuels on copper. *Innov. Mater.* **2023**, *1*, 100014. [CrossRef]
67. Zhang, R.; Li, L.; Frazer, L.; Chang, K.B.; Poeppelmeier, K.R.; Chan, M.K.; Guest, J.R. Atomistic determination of the surface structure of Cu_2O (111): Experiment and theory. *Phys. Chem. Chem. Phys.* **2018**, *20*, 27456–27463. [CrossRef] [PubMed]
68. Mishra, A.K.; Roldan, A.; de Leeuw, N.H. A density functional theory study of the adsorption behaviour of CO_2 on Cu_2O surfaces. *J. Chem. Phys.* **2016**, *145*, 044709. [CrossRef] [PubMed]
69. Xing, W.; Meng, F.; Yu, R. Atomic structure of the Cu_2O (111) surface: A transmission electron microscopy and DFT+ U study. *Phys. Status Solidi* **2021**, *258*, 2100185. [CrossRef]
70. Goos, E.; Burcat, A. Overview of thermochemistry and its application to reaction kinetics. In *Rate Constant Calculation for Thermal Reactions: Methods and Applications*; John Wiley & Sons, Inc.: Hoboken, NJ, USA, 2011; pp. 1–32. [CrossRef]
71. Ohya, S.; Kaneco, S.; Katsumata, H.; Suzuki, T.; Ohta, K. Electrochemical reduction of CO_2 in methanol with aid of CuO and Cu_2O. *Catal. Today* **2009**, *148*, 329–334. [CrossRef]
72. Shen, Y.; Qian, L.; Xu, Q.; Wang, S.; Chen, Y.; Lu, H.; Zhou, Y.; Ye, J.; Zhao, J.; Gao, X. N-doped Cu_2O with the tunable CuO and Cu^+ sites for selective CO_2 electrochemical reduction to ethylene. *J. Environ. Sci.* **2025**, *150*, 246–253. [CrossRef]
73. Yan, C.; Luo, W.; Yuan, H.; Liu, G.; Hao, R.; Qin, N.; Wang, Z.; Liu, K.; Wang, Z.; Cui, D. Stabilizing intermediates and optimizing reaction processes with N doping in Cu_2O for enhanced CO_2 electroreduction. *Appl. Catal. B Environ.* **2022**, *308*, 121191. [CrossRef]
74. Wang, Z.; Wu, J.; Wei, W.; Gao, M.; Zhang, Y.-W.; Yu, Z.G.; Liang, Y.C.; Zhu, C. Pt single-atom electrocatalysts at Cu_2O nanowires for boosting electrochemical sensing toward glucose. *Chem. Eng. J.* **2024**, *495*, 153564. [CrossRef]

75. Wang, C.; Kong, Y.; Soldemo, M.; Wu, Z.; Tissot, H.; Karagoz, B.; Marks, K.; Stenlid, J.H.; Shavorskiy, A.; Kokkonen, E. Stabilization of Cu_2O through site-selective formation of a Co1Cu hybrid single-atom catalyst. *Chem. Mater.* **2022**, *34*, 2313–2320. [CrossRef]
76. Zhao, Y.; Wang, S.; Zhu, L.J.; Sun, M.J.; Zhang, T.; Cao, R. A Graphene-Supported Copper Complex as Site-Isolated Catalyst for Electrochemical CO_2 Reduction. *ChemElectroChem* **2022**, *9*, e202200023. [CrossRef]
77. Li, J.; Meng, C.; Gu, J.; Wang, H.; Dai, R.; Sha, H.; Zhu, H. High faradic efficiency of CO_2 conversion to formic acid catalyzed by Cu_2O hollow-dices. *Carbon Neutrality* **2022**, *1*, 36. [CrossRef]
78. Fedorov, A.; Lund, H.; Kondratenko, V.A.; Kondratenko, E.V.; Linke, D. Elucidating reaction pathways occurring in CO_2 hydrogenation over Fe-based catalysts. *Appl. Catal. B Environ.* **2023**, *328*, 122505. [CrossRef]
79. Zhao, B.; Sun, M.; Chen, F.; Wang, W.; Lu, S.; Zhang, B. Photoinduced reaction pathway change for boosting CO_2 hydrogenation over a MnO-Co catalyst. *ACS Catal.* **2021**, *11*, 10316–10323. [CrossRef]
80. Huang, W. Oxide Nanocrystal Model Catalysts. *Acc. Chem. Res.* **2016**, *49*, 520–527. [CrossRef]
81. Zhang, D.-F.; Zhang, H.; Guo, L.; Zheng, K.; Han, X.-D.; Zhang, Z. Delicate control of crystallographic facet-oriented Cu 2 O nanocrystals and the correlated adsorption ability. *J. Mater. Chem.* **2009**, *19*, 5220–5225. [CrossRef]
82. Sun, Y.-F.; Liu, Z.; Liu, X.; Gan, L.-H.; Zhang, W.; Zhao, X.; Zhao, L.-B. Selective methanol production via CO_2 reduction on Cu_2O revealed by micro-kinetic study combined with constant potential model. *Appl. Surf. Sci.* **2025**, *681*, 161469. [CrossRef]
83. Liu, H.; Liu, D.; Yu, Z.; Bai, H.; Pan, H. Electrochemical reduction of CO_2 on pure and doped Cu_2O (1 1 1). *J. Colloid Interface Sci.* **2025**, *683*, 170–177. [CrossRef]
84. Mandal, L.; Yang, K.R.; Motapothula, M.R.; Ren, D.; Lobaccaro, P.; Patra, A.; Sherburne, M.; Batista, V.S.; Yeo, B.S.; Ager, J.W. Investigating the role of copper oxide in electrochemical CO_2 reduction in real time. *ACS Appl. Mater. Interfaces* **2018**, *10*, 8574–8584. [CrossRef]
85. Chang, X.; Wang, T.; Zhao, Z.J.; Yang, P.; Greeley, J.; Mu, R.; Zhang, G.; Gong, Z.; Luo, Z.; Chen, J. Tuning Cu/Cu_2O interfaces for the reduction of carbon dioxide to methanol in aqueous solutions. *Angew. Chem. Int. Ed.* **2018**, *57*, 15415–15419. [CrossRef]
86. Liu, B.; Yao, X.; Zhang, Z.; Li, C.; Zhang, J.; Wang, P.; Zhao, J.; Guo, Y.; Sun, J.; Zhao, C. Synthesis of Cu_2O Nanostructures with Tunable Crystal Facets for Electrochemical CO_2 Reduction to Alcohols. *ACS Appl. Mater. Interfaces* **2021**, *13*, 39165–39177. [CrossRef] [PubMed]
87. Castro-Castillo, C.; Nanda, K.K.; Mardones-Herrera, E.; Gazzano, V.; Ruiz-León, D.; Aguirre, M.J.; García, G.; Armijo, F.; Isaacs, M. Growth direction and exposed facets of Cu/Cu_2O nanostructures affect product selectivity in CO_2 electroreduction. *Mater. Chem. Phys.* **2022**, *278*, 125650. [CrossRef]
88. Luo, H.; Li, B.; Ma, J.G.; Cheng, P. Surface Modification of Nano-Cu_2O for Controlling CO_2 Electrochemical Reduction to Ethylene and Syngas. *Angew. Chem. Int. Ed.* **2022**, *61*, e202116736. [CrossRef] [PubMed]
89. Yuan, J.; Wang, X.; Gu, C.; Sun, J.; Ding, W.; Wei, J.; Zuo, X.; Hao, C. Photoelectrocatalytic reduction of carbon dioxide to methanol at cuprous oxide foam cathode. *RSC Adv.* **2017**, *7*, 24933–24939. [CrossRef]
90. Yang, Z.X.; Wen, X.; Gao, L.J.; Zhang, J.; Wei, R.P.; Pan, X.M.; Xiao, G.M. Facilitating CO_2 electroreduction to C_2H_4 through facile regulating {100} & {111} grain boundary of Cu_2O. *Catal. Commun.* **2023**, *174*, 106595.
91. Hazarika, J.; Manna, M.S. Electrochemical reduction of CO_2 to methanol with synthesized Cu_2O nanocatalyst: Study of the selectivity. *Electrochim. Acta* **2019**, *328*, 135053. [CrossRef]
92. Wu, J.C.; Lin, H.-M.; Lai, C.-L. Photo reduction of CO_2 to methanol using optical-fiber photoreactor. *Appl. Catal. A Gen.* **2005**, *296*, 194–200. [CrossRef]
93. Schmitt, K.G. Investigating Electrochemical Reduction Processes via In Situ Enhanced Raman Spectroscopy for Carbon Dioxide Conversion and Copper Deposition. Doctoral Dissertation, University of Illinois at Urbana-Champaign, Champaign, IL, USA, 2016.
94. Besharat, Z.; Halldin Stenlid, J.; Soldemo, M.; Marks, K.; Önsten, A.; Johnson, M.; Öström, H.; Weissenrieder, J.; Brinck, T.; Göthelid, M. Dehydrogenation of methanol on Cu_2O (100) and (111). *J. Chem. Phys.* **2017**, *146*, 244702. [CrossRef] [PubMed]
95. Yang, Y.; Fu, H.; Xiao, C.; Du, X.; Song, Z. Efficient electrochemical CO_2 reduction to C^{2+} hydrocarbons on Zn-doped Cu films. *Appl. Surf. Sci.* **2024**, *646*, 158866. [CrossRef]
96. Xue, Q.; Qi, X.; Li, K.; Zeng, Y.; Xu, F.; Zhang, K.; Qi, X.; Li, L.; Cabot, A. Axial heteroatom (P, S and Cl)-decorated Fe single-atom catalyst for the oxygen reduction reaction: A DFT study. *RSC Adv.* **2024**, *14*, 16379–16388. [CrossRef]
97. Liu, Z.; Krösschell, R.D.; Filot, I.A.; Hensen, E.J. A combined density functional theory and microkinetics simulations study of electrochemical CO_2 reduction on $Cu8/SnO_2$ (110): The crucial role of hydrogen coverage. *Electrochim. Acta* **2024**, *493*, 144409. [CrossRef]
98. Ramadhany, P.; Trần-Phú, T.; Yuwono, J.A.; Ma, Z.; Han, C.; Nguyen, T.K.A.; Leverett, J.; Kumar, P.; Hocking, R.K.; Tricoli, A. Triggering C–N Coupling on Metal Oxide Nanocomposite for the Electrochemical Reduction of CO_2 and NOx^- to Formamide. *Adv. Energy Mater.* **2024**, *14*, 2401786. [CrossRef]

99. Tripkovic, V.; Björketun, M.E.; Skúlason, E.; Rossmeisl, J. Standard hydrogen electrode and potential of zero charge in density functional calculations. *Phys. Rev. B* **2011**, *84*, 115452. [CrossRef]
100. Gong, L.; Wang, X.; Zheng, T.; Liu, J.; Wang, J.; Yang, Y.-C.; Zhang, J.; Han, X.; Zhang, L.; Xia, Z. Catalytic mechanism and design principle of coordinately unsaturated single metal atom-doped covalent triazine frameworks with high activity and selectivity for CO_2 electroreduction. *J. Mater. Chem. A* **2021**, *9*, 3555–3566. [CrossRef]

Disclaimer/Publisher's Note: The statements, opinions and data contained in all publications are solely those of the individual author(s) and contributor(s) and not of MDPI and/or the editor(s). MDPI and/or the editor(s) disclaim responsibility for any injury to people or property resulting from any ideas, methods, instructions or products referred to in the content.